Nonlinear Backstepping Controller for an Underactuated ASV With Model Parametric Uncertainty: Design and Experimental Validation

Joel Reis, Wei Xie, *Member, IEEE*, David Cabecinhas, and Carlos Silvestre, *Senior Member, IEEE*

***Abstract*—In this article, we tackle the problem of path following control of an underactuated autonomous surface vehicle in the presence of external disturbances and model parametric uncertainty. Using the conventional Lyapunov-based backstepping technique, we derive a nonlinear control law to determine a vectored actuation composed of a thrust direction and a thrust force that is bounded with respect to the position error. The model's linear and angular hydrodynamic damping terms are assumed to be known with uncertainty, while the external disturbances are fully unknown. The errors stemming from both the model parametric uncertainty and the exogenous disturbances are compensated by a couple of bounded integral actions which, when embedded into the control law, help rendering the origin of the error system a global attractor. The proposed strategy is validated by a set of simulation results, with its efficacy and robustness further demonstrated through a set of experimental trials using a fully autonomous instrumented surface craft.**

***Index Terms*—Underactuated autonomous vehicles, robust nonlinear control, model parametric uncertainty.**

I. Introduction

THE continued development of autonomous surface vehicles (ASVs) has been driven by an imposition to reduce both mission costs and operational risks, which is invariably attained by removing humans from the scene. This notwithstanding, the ceaseless technological advances in the fields of batteries and low-cost inertial and positioning sensors have made ASVs more affordable, and simultaneously more versatile. This steady trend has expanded ASVs' range of applications and, consequently, brought them closer to interdisciplinary fields [1]. However, as claimed in the brief historical overview of unmanned surface crafts presented in [2], despite the proliferation of proven ASV prototypes, the market is yet to see an influx of these marine autonomous robots. This might be due to the downside of the many special challenges that exist in marine environments that are not present in ground and aerial robotics [3], meaning that ASVs remain the target of an active and in-depth, practical and theoretical research.

One of the key purposes of ASVs is to safely automatize the monitoring of marine environments. Collecting relevant data, e.g., bathymetric charts, water quality profiles, reports on structural damages to underwater tunnels and pillars, etc., requires the vehicle to follow, sometimes repeatedly, a predetermined curve with high accuracy. Among a vast literature on trajectory tracking and path following, the reader is referred to [4], [5], [6], [7], [8], [9], and the references therein.

Some approaches to solve the problem of path following draw inspiration from ocean navigators, who intuitively resort to line-of-sight (LOS) for guidance purposes. See, e.g., [10], [11] and [12], where the authors present LOS algorithms for navigation of autonomous underactuated vehicles. In particular, the solution in [11] is capable of canceling the effects of constant environmental disturbances, such as ocean currents. Similarly, [12] combines an ocean current observer and a controller based on a LOS-like guidance by considering a global parameterization of the general curved path. Compensating the constant bias of environmental disturbances is also addressed in [13], where integral actions are added to the controller. For further more general methodologies that employ neural networks and reinforcement learning please refer, e.g., to [14], [15] and the references therein.

Over the years, the multifaceted Lyapunov theory found its way into several branches of robotics, in particular, nonlinear control of autonomous vehicles. In the recent work [16], a surface vessel subject to unknown disturbances caused by current, waves and wind is controlled by an algorithm based on a new barrier Lyapunov function that is designed for the error to not exceed a prescribed constraint. In [17], the control objective is

Manuscript received 10 October 2022; revised 31 October 2022; accepted 9 November 2022. Date of publication 14 November 2022; date of current version 27 April 2023. The work of Joel Reis was supported by the FDCT Funding Scheme for Postdoctoral Researchers of Higher Education Institutions 2021 under Grant 0030/2021/APD. The work of David Cabecinhas was supported by FCT Scientific Employment Stimulus under Grant CEECIND/04199/2017. This work was supported in part by Macau Science and Technology Development Fund under Grant FDCT/0146/2019/A3, in part by the Projects MYRG2018-00198-FST and MYRG2020-00188-FST of the University of Macau, by LARSyS FCT Project under Grant UIDB/50009/2020, in part by the National Natural Science Foundation of China under Grant 62203297, and in part by Shanghai Sailing Program under Grant 22YF1420400. *(Corresponding author: Wei Xie.)*

Joel Reis is with the Department of Electrical and Computer Engineering of the Faculty of Science and Technology, University of Macau, Taipa 999078, China (e-mail: joelreis@um.edu.mo).

Wei Xie is with the Department of Automation, Shanghai Jiao Tong University, Shanghai 200240, China (e-mail: weixie@sjtu.edu.cn).

David Cabecinhas is with the Institute for Systems and Robotics, Instituto Superior Técnico, Universidade de Lisboa, 1049–001 Lisboa, Portugal (e-mail: dcabecinhas@isr.ist.utl.pt).

Carlos Silvestre is with the Department of Electrical and Computer Engineering of the Faculty of Science and Technology, University of Macau, Taipa, Macao, on leave from the Instituto Superior Técnico, Universidade de Lisboa, Lisboa, Portugal (e-mail: csilvestre@um.edu.mo).

Color versions of one or more figures in this article are available at https://doi.org/10.1109/TIV.2022.3221739.

Digital Object Identifier 10.1109/TIV.2022.3221739

to reach and closely follow a pre-specified trajectory, operating in an environment perturbed by currents and waves; therein, the authors propose a control scheme based on the interaction of guidance laws synthesized by Lyapunov techniques and a high order sliding mode control approach based on the Super Twisting Algorithm. In [9], a change of coordinates, which is not standard for the input–output feedback linearizing approach, is presented that helps to obtain a transformed model where the ocean current affects the system at the level of the linear external dynamics and can be compensated by a simple integral action.

The motivation for this research is shared by virtually all control applications for marine crafts: to design robust controllers that can handle unmodeled/incomplete dynamics. The handbook [18] offers an extensive overview on how to analyze and design kinematic and dynamic models for surface and underwater vehicles.

However, any mathematical model is ultimately an approximation of reality. Furthermore, an accurate identification of the model's physical parameters, e.g., hydrodynamic drag/damping coefficients, is quite a challenging task.

II. Related Work

There are two paradigms of parameter identification: online and offline. The work in [19] discusses some of the caveats associated with the latter. In [20], parameters are identified using a least squares support vector machine, which is widely used in identification of ship hydrodynamic coefficients. In [21], the parameters of the proposed adaptive near-optimal control laws are updated in a real-time manner without the need for an offline training. In [22], the uncertainties of dynamics are compensated by using a robust adaptive radial basis function neural network. Similarly, [23] also introduces neural networks in the control algorithm to reject the influence of uncertainties, with the lack of knowledge about the plant nonlinearities being lessened by offline training of the neural networks to the unknown nonlinearities in advance. Without considering external disturbances, the strategy proposed in [24] uses integral concurrent learning to render a closed loop system globally exponentially stable with exponential identification of the unknown parameters online without persistence of excitation. However, the achieved performance level, in simulation, lags behind the required one in most of the missions which ASVs are designed for. In [4], the authors propose a multi-estimator-based supervisory control architecture to handle model parametric uncertainty, but without considering external disturbances.

In previous work by the authors [25], the problem of trajectory tracking using an underactuated ASV was addressed considering external disturbances. The contributions of this paper may be summarized as follows: i) both external disturbances and model parametric uncertainty are considered whose impact is counteracted resorting to bounded integral action; ii) this action is embedded into a control law, bounded with respect to the position error, that is derived using the conventional Lyapunov-based backstepping technique, rendering the origin of the resulting error system a global attractor; iii) we analyze the stability of the vessel's zero dynamics, an overlooked issue in most of the related literature; iv) we present a Monte Carlo study to support the theoretical findings resulting from the analysis of the vessel's zero dynamics; v) our path following control strategy is validated by an extensive set of simulations, and experimental results obtained using an instrumented ASV operating in a lake in the presence of wind and water currents.

A. Notation

Throughout this paper, bold symbols stand for multidimensional variables. The n-dimensional Euclidean space is represented by $\mathbb{R}^n$. The symbol $\mathbf{I}$ denotes the identity matrix of appropriate dimensions. A function f is of class $\mathcal{C}^n$ if its derivatives $f,' f,'' \ldots, f^{(n)}$ exist and are continuous. Given a vector $\mathbf{x} \in \mathbb{R}^n$: i) its norm is defined as $\|\mathbf{x}\| = \sqrt{\mathbf{x}^{\mathrm{T}}\mathbf{x}}$, where the superscript $(\cdot)^{\mathrm{T}}$ denotes the transpose operator; ii) its estimate/approximation is denoted by $\hat{\mathbf{x}}$; and iii) its corresponding error/deviation is defined as $\tilde{\mathbf{x}} := \mathbf{x} - \hat{\mathbf{x}}$. The binary operator $\odot$ represents the Hadamard (element-wise) product. The operator $\mathrm{diag}(\mathbf{x})$ returns a square matrix with the elements of $\mathbf{x}$ along the main diagonal. The trace of a matrix is denoted by $\mathrm{tr}(\cdot)$. The operators $\min(\cdot)$ and $\max(\cdot)$ return the smallest and largest values, respectively, of their operands. The two-dimensional matrix skew operator is denoted by $\mathbf{S} = [0, -1; 1, 0] \in \mathbb{R}^{2\times 2}$. The special orthogonal group of order two is denoted by $\mathsf{SO}(2) := \{\mathbf{X} \in \mathbb{R}^{2\times 2} : \mathbf{X}\mathbf{X}^{\mathsf{T}} = \mathbf{X}^{\mathsf{T}}\mathbf{X} = \mathbf{I}, \det(\mathbf{X}) = 1\}$. Finally, for convenience, $\mathbf{u}_1, \mathbf{u}_2 \in \mathbb{R}^2$ are orthonormal vectors defined as $\mathbf{u}_1 := [1, 0]^{\mathsf{T}}$ and $\mathbf{u}_2 := [0, 1]^{\mathsf{T}}$.

III. Problem Formulation

A. ASV Dynamic Modeling

Consider an underactuated ASV modeled as a rigid body of mass $m > 0$ subjected to constant inertial forces and torques. The source of these disturbances can be attributed, e.g., to water currents and wind. Let us choose two frames: an inertial one denoted by $\{I\}$, and a body-fixed one, denoted by $\{B\}$, whose origin coincides with the vessel's center of mass.

Let $\mathbf{p}(t) \in \mathbb{R}^2$ denote the inertial coordinates of the vehicle's center of mass, and let $\psi(t) \in [-\pi, \pi]$ denote its orientation. The ASV's linear and angular velocities, both expressed in $\{B\}$, are represented by $\mathbf{v}(t) \in \mathbb{R}^2$ and by $r(t) \in \mathbb{R}$, respectively. The kinematics describing the ASV's motion thus follows as

$$\begin{cases} \dot{\mathbf{p}}(t) = \mathbf{R}(t)\mathbf{v}(t), & \text{(1a)} \\ \dot{\mathbf{R}}(t) = r(t)\mathbf{R}(t)\mathbf{S}, & \text{(1b)} \end{cases}$$

where $\mathbf{R}(t) \in \mathsf{SO}(2)$ is the rotation matrix from $\{B\}$ to $\{I\}$. When parameterized by $\psi(t)$, we can write $\mathbf{R}(\psi) = [\cos(\psi), -\sin(\psi); \sin(\psi), \cos(\psi)]$.

Consider now that the ASV is actuated by a vectored thrust force $\mathbf{T}(t) \in \mathbb{R}^2$ that produces a torque $\tau(t) \in \mathbb{R}$ because the force is not applied to the center of gravity. As for the vehicle's physical constants, let $X_{\dot{u}}, Y_{\dot{v}} \in \mathbb{R}$ denote added masses, $\mathbf{d}_l \in \mathbb{R}^2$ and $d_r \in \mathbb{R}$ denote positive linear damping coefficients, and, finally, let $\mathbf{d}_q \in \mathbb{R}^2$ and $d_{r|r|} \in \mathbb{R}$ denote positive quadratic

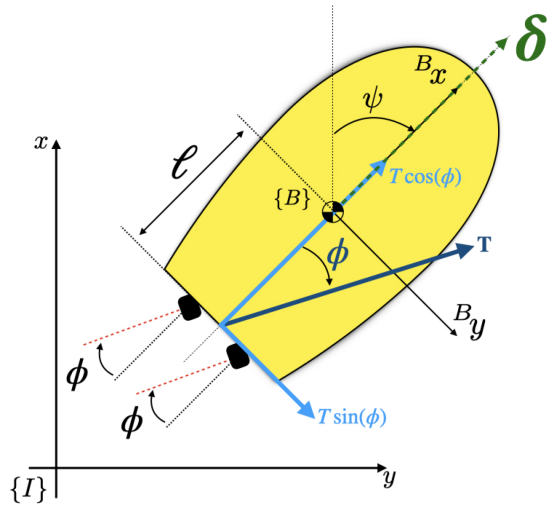

Fig. 1. Coordinate systems and stylized sketch of the ASV.

damping coefficients[1]. The ASV's dynamic equations can thus be written as

$$\begin{cases} \mathbf{M}\dot{\mathbf{v}}(t) = -\left(r(t)\mathbf{SM} + \mathbf{D}_l\right)\mathbf{v}(t) - \mathbf{D}_q\mathbf{v}(t) \odot |\mathbf{v}(t)| \\ \quad + \mathbf{T}(t) + \mathbf{R}^{\mathsf{T}}(t)\,{}^I\mathbf{b}_{\mathbf{v}} & \text{(2a)} \\ J\dot{r}(t) = -d_r r(t) - d_{r|r|} r(t)|r(t)| + \tau(t) + b_r, & \text{(2b)} \end{cases}$$

where $\mathbf{M} := \mathrm{diag}(m - X_{\dot{u}},\, m - Y_{\dot{v}}) \in \mathbb{R}^{2\times 2}$ is a positive definite mass matrix, $\mathbf{D}_l := \mathrm{diag}(\mathbf{d}_l) \in \mathbb{R}^{2\times 2}$, $\mathbf{D}_q := \mathrm{diag}(\mathbf{d}_q) \in \mathbb{R}^{2\times 2}$, $J \in \mathbb{R}$ is the rotational inertia moment about the z axis, and where ${}^I\mathbf{b}_{\mathbf{v}} \in \mathbb{R}^2$ and $b_r \in \mathbb{R}$ denote external disturbances.

Assuming the ASV equipped with a clockwise and a counter-clockwise propeller, and both propellers working at the same rotational speed, the angle of the thrust vector, denoted by $\phi(t) \in [-\pi/2,\, \pi/2]$, is changed by using the motor angle. It follows, based on Fig. 1, that

$$\mathbf{T}(t) = T(t)\left[\cos(\phi(t)), \sin(\phi(t))\right]^{\mathsf{T}} \text{ and}$$
$$\tau(t) = -T(t)\sin(\phi(t))\ell = -\mathbf{u}_2^{\mathsf{T}}\mathbf{T}(t)\ell,$$

where $T(t) = \|\mathbf{T}(t)\|$ is the force generated by the propellers and ℓ is the torque arm length. Note that the function which maps the set $(\phi(t), T(t))$ onto $\mathbf{T}(t)$ is a bijection, meaning that working on either set is equivalent.

In this work, we assume that the external disturbances ${}^I\mathbf{b}_v$ and b_r are unknown, while realistically the model parameters are known with uncertainty.

By construction, the physical parameters are positive. Moreover, thanks to preliminary model identifications, we have a rough estimate of their magnitude and weight relative to one another. In other words, each model parameter can be expressed as the sum of a known term together with a variable conveying a bounded uncertainty. Hence, let us gather the linear and angular uncertainties and the external disturbances into single (unknown and constant) vectors as

$$\boldsymbol{\theta}_{\mathbf{v}} := \begin{bmatrix} \boldsymbol{\theta}_l^{\mathsf{T}} & \boldsymbol{\theta}_q^{\mathsf{T}} & {}^I\mathbf{b}_v^{\mathsf{T}} \end{bmatrix}^{\mathsf{T}} \in \mathbb{R}^6 \text{ and } \boldsymbol{\theta}_r := \begin{bmatrix} \theta_r & \theta_{r|r|} & b_r \end{bmatrix}^{\mathsf{T}} \in \mathbb{R}^3.$$

Likewise, let

$$\bar{\boldsymbol{\phi}}_v := \begin{bmatrix} \bar{\mathbf{d}}_l^{\mathsf{T}} & \bar{\mathbf{d}}_q^{\mathsf{T}} & \mathbf{0} \end{bmatrix}^{\mathsf{T}} \in \mathbb{R}^6 \text{ and } \bar{\boldsymbol{\phi}}_r := \begin{bmatrix} \bar{d}_r & \bar{d}_{r|r|} & 0 \end{bmatrix}^{\mathsf{T}} \in \mathbb{R}^3$$

be (known and constant) vectors containing our own estimates of the model parameters. As result, the dynamic model (2) can be rewritten compactly as

$$\begin{cases} \dot{\mathbf{v}}(t) = -r(t)\mathbf{M}^{-1}\mathbf{SM}\mathbf{v}(t) - \boldsymbol{\Phi}_{\mathbf{v}}(\mathbf{v}, \mathbf{R})\boldsymbol{\phi}_{\mathbf{v}} + \mathbf{M}^{-1}\mathbf{T}(t) \\ \dot{r}(t) = -\mathbf{u}_2^{\mathsf{T}}\mathbf{T}(t)\ell/J - \boldsymbol{\Phi}_r(r)\boldsymbol{\phi}_r, \end{cases}$$

where

$$\boldsymbol{\Phi}_{\mathbf{v}}(\mathbf{v}, \mathbf{R}) := \mathbf{M}^{-1}\begin{bmatrix} \mathrm{diag}(\mathbf{v}(t)) \\ \mathrm{diag}(\mathbf{v}(t) \odot |\mathbf{v}(t)|) \\ -\mathbf{R}(t) \end{bmatrix}^{\mathsf{T}} \in \mathbb{R}^{2\times 6},$$
$$\boldsymbol{\Phi}_r(r) := J^{-1}\left[r(t),\, r(t)|r(t)|,\, -1\right] \in \mathbb{R}^{1\times 3}, 3 \quad (4)$$

and, finally, where

$$\boldsymbol{\phi}_{\mathbf{v}} := \bar{\boldsymbol{\phi}}_{\mathbf{v}} + \boldsymbol{\theta}_{\mathbf{v}} \text{ and } \boldsymbol{\phi}_r := \bar{\boldsymbol{\phi}}_r + \boldsymbol{\theta}_r.$$

B. Problem Statement

Consider a reference trajectory described by a parameterized curve $\mathbf{p}_d(\gamma) \in \mathbb{R}^2$ that is of class at least $\mathcal{C}^2$, and whose time derivatives are all bounded, given a certain speed profile $\gamma(t)$. Our control objective consists in designing a control law for both $T(t)$ and $\phi(t)$, i.e., $\mathbf{T}(t)$, that ensures convergence of a fixed point in the vehicle's body frame, given by $\boldsymbol{\delta} = [\delta_x, 0]^{\mathsf{T}} \in \mathbb{R}^2$, with $\delta_x > 0$, to the neighborhood of the desired trajectory $\mathbf{p}_d(\gamma)$ with an arbitrarily small position error given by $\|\mathbf{p}(t) - \mathbf{p}_d(\gamma) + \mathbf{R}(t)\boldsymbol{\delta}\|$. Informally, this can be seen as if a virtual vehicle is pulling the ASV like a trailer.

IV. Path Following Controller Design

Inspired by [4], let us define the first state of our error system, i.e., the position error, expressed in $\{I\}$, as

$$\mathbf{z}_1(t) := \mathbf{p}(t) - \mathbf{p}_d(\gamma) + \mathbf{R}(t)\boldsymbol{\delta} \in \mathbb{R}^2. \quad (5)$$

Consider now the first candidate Lyapunov function given by

$$V_1(\mathbf{z}_1) := \kappa_{\max}\left[\sqrt{\|\mathbf{z}_1(t)\|^2 + 1} - 1\right],$$

where $\kappa_{\max}$ is a positive scalar. Using (1a) and (5), the time derivative of $V_1(\mathbf{z}_1)$ follows as

$$\frac{d}{dt}V_1(\mathbf{z}_1) = \left[\mathbf{R}^{\mathsf{T}}(t)\sigma(\mathbf{z}_1)\right]^{\mathsf{T}}\left[\mathbf{v}(t) - \mathbf{R}^{\mathsf{T}}(t)\dot{\mathbf{p}}_d(\gamma) + r(t)\mathbf{S}\boldsymbol{\delta}\right], \quad (6)$$

[1]The hydrodynamic parameters and added mass terms are based on the dynamic models described in [18].

where $\sigma(\mathbf{z}_1) : \mathbb{R}^2 \to \mathbb{R}^2$ is a saturation function defined as

$$\sigma(\mathbf{z}_1) := \kappa_{\max} \frac{\mathbf{z}_1(t)}{\sqrt{\|\mathbf{z}_1(t)\|^2 + 1}}. \tag{7}$$

From (7), we can write down the following partial derivative, which will be useful in the sequel:

$$\frac{\partial \sigma(\mathbf{z}_1)}{\partial \mathbf{z}_1} = \frac{\kappa_{\max}}{\sqrt{\|\mathbf{z}_1(t)\|^2 + 1}} \left[\mathbf{I} - \frac{\sigma(\mathbf{z}_1)\sigma^{\mathsf{T}}(\mathbf{z}_1)}{\kappa_{\max}^2} \right].$$

As result, the time derivative of $\sigma(\mathbf{z}_1)$, also useful in the sequel, follows, from (1a) and (5), as

$$\frac{d}{dt}\sigma(\mathbf{z}_1) = \frac{\partial \sigma(\mathbf{z}_1)}{\partial \mathbf{z}_1} \left[\mathbf{R}(t)\mathbf{v}(t) - \dot{\mathbf{p}}_d(\gamma) + r(t)\mathbf{R}(t)\mathbf{S}\boldsymbol{\delta} \right].$$

Let $Z_1(\mathbf{z}_1) : \mathbb{R}^2 \to \mathbb{R}$ be a positive definite function defined as

$$Z_1(\mathbf{z}_1) := k_1 \|\sigma(\mathbf{z}_1)\|^2.$$

On the right-hand side of (6), proceed to add and subtract $Z_1(\mathbf{z}_1)$. After rearranging its elements, (6) can be rewritten as

$$\frac{d}{dt}V_1(\mathbf{z}_1) = -Z_1(\mathbf{z}_1) + \left[\mathbf{R}^{\mathsf{T}}(t)\sigma(\mathbf{z}_1)\right]^{\mathsf{T}} \mathbf{z}_2(t),$$

where $\mathbf{z}_2(t) \in \mathbb{R}^2$ is the second, and last state of our error system, this time expressed in $\{B\}$, and defined as

$$\mathbf{z}_2(t) := \mathbf{v}(t) - \mathbf{R}^{\mathsf{T}}(t)\dot{\mathbf{p}}_d(\gamma) + k_1\mathbf{R}^{\mathsf{T}}(t)\sigma(\mathbf{z}_1) + r(t)\mathbf{S}\boldsymbol{\delta}, \tag{8}$$

Adopting the backstepping approach, define a new candidate Lyapunov function as

$$V_2(\mathbf{z}_1, \mathbf{z}_2) := V_1(\mathbf{z}_1) + \frac{1}{2}\mathbf{z}_2^{\mathsf{T}}(t)\mathbf{M}\mathbf{z}_2(t). \tag{9}$$

In turn, the time derivative of (9), after straightforward algebraic manipulations, can be written as

$$\begin{aligned}
\frac{d}{dt}V_2(\mathbf{z}_1, \mathbf{z}_2) = & -Z_2(\mathbf{z}_1, \mathbf{z}_2) \\
& + \mathbf{z}_2^{\mathsf{T}}(t)\{-r(t)\mathbf{S}\mathbf{M}\mathbf{v}(t) \\
& + \left(\mathbf{I} - \ell/J\mathbf{M}\mathbf{S}\boldsymbol{\delta}\mathbf{u}_2^{\mathsf{T}}\right)\mathbf{T}(t) + k_2\mathbf{z}_2(t) \\
& + \mathbf{M}\mathbf{S}\mathbf{R}^{\mathsf{T}}(t)\dot{\mathbf{p}}_d(\gamma)r(t) - \mathbf{M}\mathbf{R}^{\mathsf{T}}(t)\ddot{\mathbf{p}}_d(\gamma) \\
& + k_1\mathbf{M}\mathbf{R}^{\mathsf{T}}(t)\frac{d}{dt}\sigma(\mathbf{z}_1) \\
& + \left[\mathbf{I} - k_1 r(t)\mathbf{M}\mathbf{S}\right]\mathbf{R}^{\mathsf{T}}(t)\sigma(\mathbf{z}_1) \\
& - \mathbf{M}\boldsymbol{\Phi}_{\mathbf{v}}(\mathbf{v}, \mathbf{R})\left(\bar{\phi}_{\mathbf{v}} + \boldsymbol{\theta}_{\mathbf{v}}\right) \\
& - \mathbf{M}\mathbf{S}\boldsymbol{\delta}\boldsymbol{\Phi}_r(r)\left(\bar{\phi}_r + \boldsymbol{\theta}_r\right)\},
\end{aligned} \tag{10}$$

where, for positive scalar k_2, the positive definite function $Z_2(\mathbf{z}_1, \mathbf{z}_2) : \mathbb{R}^2 \times \mathbb{R}^2 \to \mathbb{R}$ is defined as

$$Z_2(\mathbf{z}_1, \mathbf{z}_2) := Z_1(\mathbf{z}_1) + k_2\|\mathbf{z}_2(t)\|^2.$$

The introduction of $Z_2(\mathbf{z}_1, \mathbf{z}_2)$ will be useful to demonstrate the controller's global convergence properties.

We cannot include $\mathbf{T}(t)$, $\boldsymbol{\theta}_{\mathbf{v}}$ and $\boldsymbol{\theta}_r$ in the control laws for they represent unknown quantities. In this work, however, the purpose is not to estimate precisely the model parametric uncertainties or the external disturbances, but rather to show that the controller is robust to them. Our strategy will thus consist in introducing an integral action to help the controller eliminate offsets associated with $\boldsymbol{\theta}_{\mathbf{v}}$ and $\boldsymbol{\theta}_r$.

Assumption 1: The model parametric uncertainties and the external disturbances are unknown, constant, and bounded, satisfying $\|\boldsymbol{\theta}_{\mathbf{v}}\| \leq \zeta_v$ and $\|\boldsymbol{\theta}_r\| \leq \zeta_r$, for known $\zeta_v, \zeta_r > 0$.

This assumption is reasonable in a practical sense: the energy of dynamical systems is limited.

Consider the decompositions

$$\boldsymbol{\theta}_{\mathbf{v}} = \hat{\boldsymbol{\theta}}_{\mathbf{v}}(t) + \tilde{\boldsymbol{\theta}}_{\mathbf{v}}(t) \text{ and } \boldsymbol{\theta}_r = \hat{\boldsymbol{\theta}}_r(t) + \tilde{\boldsymbol{\theta}}_r(t),$$

where both constant vectors, i.e., $\boldsymbol{\theta}_{\mathbf{v}}$ and $\boldsymbol{\theta}_r$, are split up into two time-varying components to be defined in the sequel with the help of a third candidate Lyapunov function given by

$$\begin{aligned}
V_3(\tilde{\boldsymbol{\theta}}_{\mathbf{v}}, \tilde{\boldsymbol{\theta}}_r, \mathbf{z}_1, \mathbf{z}_2) := & \, V_2(\mathbf{z}_1, \mathbf{z}_2) \\
& + \frac{1}{2}\tilde{\boldsymbol{\theta}}_{\mathbf{v}}^{\mathsf{T}}(t)\Lambda_{\mathbf{v}}^{-1}\tilde{\boldsymbol{\theta}}_{\mathbf{v}}(t) + \frac{1}{2}\tilde{\boldsymbol{\theta}}_r^{\mathsf{T}}(t)\Lambda_r^{-1}\tilde{\boldsymbol{\theta}}_r(t).
\end{aligned} \tag{11}$$

The time derivative of (11), according to (10), follows as

$$\begin{aligned}
& \frac{d}{dt}V_3(\tilde{\boldsymbol{\theta}}_{\mathbf{v}}, \tilde{\boldsymbol{\theta}}_r, \mathbf{z}_1, \mathbf{z}_2) = -Z_2(\mathbf{z}_1, \mathbf{z}_2) \\
& + \mathbf{z}_2^{\mathsf{T}}(t)\left\{-r(t)\mathbf{S}\mathbf{M}\mathbf{v}(t) + \left(\mathbf{I} - \ell/J\mathbf{M}\mathbf{S}\boldsymbol{\delta}\mathbf{u}_2^{\mathsf{T}}\right)\mathbf{T}(t) + k_2\mathbf{z}_2(t)\right. \\
& + \mathbf{M}\mathbf{S}\mathbf{R}^{\mathsf{T}}(t)\dot{\mathbf{p}}_d(\gamma)r(t) - \mathbf{M}\mathbf{R}^{\mathsf{T}}(t)\ddot{\mathbf{p}}_d(\gamma) \\
& + k_1\mathbf{M}\mathbf{R}^{\mathsf{T}}(t)\frac{d}{dt}\sigma(\mathbf{z}_1) + \left(\mathbf{I} - k_1 r(t)\mathbf{M}\mathbf{S}\right)\mathbf{R}^{\mathsf{T}}(t)\sigma(\mathbf{z}_1) + \\
& \left. - \mathbf{M}\boldsymbol{\Phi}_{\mathbf{v}}(\mathbf{v}, \mathbf{R})\left[\bar{\phi}_{\mathbf{v}} + \hat{\boldsymbol{\theta}}_{\mathbf{v}}(t)\right] - \mathbf{M}\mathbf{S}\boldsymbol{\delta}\boldsymbol{\Phi}_r(r)\left[\bar{\phi}_r + \hat{\boldsymbol{\theta}}_r(t)\right]\right\} \\
& - \tilde{\boldsymbol{\theta}}_{\mathbf{v}}^{\mathsf{T}}(t)\left[\boldsymbol{\Phi}_{\mathbf{v}}^{\mathsf{T}}(\mathbf{v}, \mathbf{R})\mathbf{M}\mathbf{z}_2(t) + \Lambda_{\mathbf{v}}^{-1}\dot{\hat{\boldsymbol{\theta}}}_{\mathbf{v}}(t)\right] \\
& - \tilde{\boldsymbol{\theta}}_r^{\mathsf{T}}(t)\left[-\boldsymbol{\Phi}_r^{\mathsf{T}}(r)\boldsymbol{\delta}^{\mathsf{T}}\mathbf{S}\mathbf{M}\mathbf{z}_2(t) + \Lambda_r^{-1}\dot{\hat{\boldsymbol{\theta}}}_r(t)\right],
\end{aligned} \tag{12}$$

where we used the fact that $\dot{\tilde{\boldsymbol{\theta}}}_{\mathbf{v}}(t) = -\dot{\hat{\boldsymbol{\theta}}}_{\mathbf{v}}(t)$ and $\dot{\tilde{\boldsymbol{\theta}}}_r(t) = -\dot{\hat{\boldsymbol{\theta}}}_r(t)$.

Aiming at rendering the derivative of V_3 negative definite, we implement an integral action to cancel the terms multiplying $\tilde{\boldsymbol{\theta}}_{\mathbf{v}}(t)$ and $\tilde{\boldsymbol{\theta}}_r(t)$. According to (12), we set

$$\dot{\hat{\boldsymbol{\theta}}}_{\mathbf{v}}(t) = -\Lambda_{\mathbf{v}}\boldsymbol{\Phi}_{\mathbf{v}}^{\mathsf{T}}(\mathbf{v}, \mathbf{R})\mathbf{M}\mathbf{z}_2(t) \tag{13}$$

and

$$\dot{\hat{\boldsymbol{\theta}}}_r(t) = \Lambda_r\boldsymbol{\Phi}_r^{\mathsf{T}}(r)\boldsymbol{\delta}^{\mathsf{T}}\mathbf{S}\mathbf{M}\mathbf{z}_2(t). \tag{14}$$

In spite of Assumption 1 holding, a straightforward implementation of the integral action given by (13) and (14) can lead to the windup phenomenon, which results in excess overshooting of the accumulated errors. Therefore, to ensure that both integral terms remain below pre-determined bounds, a smooth projection operator is employed, adapted from the work in [26]. Start by considering the compact convex set $\Omega := \{\mathbf{x} : \|\mathbf{x}\| \leq \zeta_{\mathbf{x}}\}$, where $\zeta_{\mathbf{x}} > 0$ is known. The projection operator is given by

$$\mathrm{Proj}(\mathbf{m}, \hat{\mathbf{x}}) = \mathbf{m} - \frac{\eta_1\eta_2}{2\left(\varepsilon^2 + 2\varepsilon\zeta_{\mathbf{x}}\right)^{n+1}\zeta_{\mathbf{x}}^2}\hat{\mathbf{x}}, \tag{15}$$

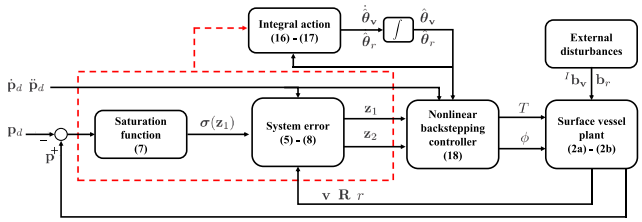

Fig. 2. Control flow diagram.

where $\hat{\mathbf{x}}$ corresponds to an approximation of $\mathbf{x}$, $\mathbf{m}$ is a known variable of class $\mathcal{C}^n$, ε is an arbitrary positive constant and

$$\eta_1 = \begin{cases} \left(\hat{\mathbf{x}}^\mathsf{T}\hat{\mathbf{x}} - \zeta_{\mathbf{x}}^2\right)^{n+1}, & \text{if } \hat{\mathbf{x}}^\mathsf{T}\hat{\mathbf{x}} - \zeta_{\mathbf{x}}^2 > 0 \\ 0, & \text{otherwise} \end{cases}$$

$$\eta_2 = \hat{\mathbf{x}}^\mathsf{T}\mathbf{m} + \sqrt{\left(\hat{\mathbf{x}}^\mathsf{T}\mathbf{m}\right)^2 + \epsilon^2},$$

with $\epsilon > 0$ being another arbitrary constant. If the initial value $\hat{\mathbf{x}}(0) \in \Omega$, then, for $\tilde{\mathbf{x}} := \mathbf{x} - \hat{\mathbf{x}} \in \mathbb{R}^2$, the projector has the following properties (cf. [26, Theorem 1]):

1) $\|\hat{\mathbf{x}}(t)\| \leq \zeta_{\mathbf{x}} + \varepsilon \quad \forall t \geq 0$;
2) $\tilde{\mathbf{x}}^\mathsf{T} \operatorname{Proj}(\mathbf{m}, \hat{\mathbf{x}}) \geq \tilde{\mathbf{x}}^\mathsf{T}\mathbf{m}$;
3) $\|\operatorname{Proj}(\mathbf{m}, \hat{\mathbf{x}})\| \leq \|\mathbf{m}\|[1 + (\frac{\zeta_{\mathbf{x}}+\varepsilon}{\zeta_{\mathbf{x}}})^2] + \epsilon\frac{\zeta_{\mathbf{x}}+\varepsilon}{2\zeta_{\mathbf{x}}^2}$;
4) $\operatorname{Proj}(\mathbf{m}, \hat{\mathbf{x}})$ if of class $\mathcal{C}^n$.

Hence, by applying the projector (15) to the integral actions (13) and (14), we obtain

$$\dot{\hat{\boldsymbol{\theta}}}_{\mathbf{v}}(t) = -\Lambda_{\mathbf{v}} \operatorname{Proj}(\boldsymbol{\Phi}_{\mathbf{v}}^\mathsf{T}(\mathbf{v}, \mathbf{R})\mathbf{M}\mathbf{z}_2(t), \hat{\boldsymbol{\theta}}_{\mathbf{v}}(t)) \tag{16}$$

and

$$\dot{\hat{\boldsymbol{\theta}}}_r(t) = \Lambda_r \operatorname{Proj}(\boldsymbol{\Phi}_r^\mathsf{T}(r)\boldsymbol{\delta}^\mathsf{T}\mathbf{S}\mathbf{M}\mathbf{z}_2(t), \hat{\boldsymbol{\theta}}_r(t)). \tag{17}$$

In order for the above properties to be valid, we choose the initial conditions of (16) and (17) to be such that $\|\hat{\boldsymbol{\theta}}_{\mathbf{v}}(0)\| \leq \zeta_{\mathbf{v}}$ and $\|\hat{\boldsymbol{\theta}}_r(0)\| \leq \zeta_r$, as suggested by Assumption 1.

Finally, from (12), we set $\mathbf{T}(t)$ such that

$$\mathbf{T}(t) = \left[\mathbf{I} - \mathbf{M}\mathbf{S}\boldsymbol{\delta}\mathbf{u}_2^\mathsf{T}\ell/J\right]^{-1}\mathbf{h}(t), \tag{18}$$

with

$$\mathbf{h}(t) := r(t)\mathbf{S}\mathbf{M}\mathbf{v}(t) + \mathbf{M}\mathbf{R}^\mathsf{T}(t)\ddot{\mathbf{p}}_d(\gamma) - \mathbf{M}\mathbf{S}\mathbf{R}^\mathsf{T}(t)\dot{\mathbf{p}}_d(\gamma)r(t)$$
$$-k_2\mathbf{z}_2(t) - k_1\mathbf{M}\mathbf{R}^\mathsf{T}(t)\frac{d}{dt}\sigma(\mathbf{z}_1) - [\mathbf{I} - k_1 r(t)\mathbf{M}\mathbf{S}]\,\mathbf{R}^\mathsf{T}(t)\sigma(\mathbf{z}_1)$$
$$+ \mathbf{M}\boldsymbol{\Phi}_{\mathbf{v}}(\mathbf{v}, \mathbf{R})\left[\bar{\boldsymbol{\phi}}_{\mathbf{v}} + \hat{\boldsymbol{\theta}}_{\mathbf{v}}(t)\right] + \mathbf{M}\mathbf{S}\boldsymbol{\delta}\boldsymbol{\Phi}_r(r)\left[\bar{\phi}_r + \hat{\boldsymbol{\theta}}_r(t)\right].$$

Using the Sherman–Morrison formula, it follows that

$$\left[\mathbf{I} - \mathbf{M}\mathbf{S}\boldsymbol{\delta}\mathbf{u}_2^\mathsf{T}\ell/J\right]^{-1} = \mathbf{I} + \frac{\mathbf{M}\mathbf{S}\boldsymbol{\delta}\ell}{J - \mathbf{u}_2^\mathsf{T}\mathbf{M}\mathbf{S}\boldsymbol{\delta}\ell}\mathbf{u}_2^\mathsf{T}. \tag{19}$$

The condition for invertibility in (19) is thus given by

$$J - \mathbf{u}_2^\mathsf{T}\mathbf{M}\mathbf{S}\boldsymbol{\delta}\ell \neq 0 \Rightarrow \delta_x \neq \frac{J}{\ell\,(m - Y_{\dot{v}})} > 0. \tag{20}$$

A depiction of the control-flow diagram is shown in Fig. 2.

The convergence properties of the proposed solution for the problem of path following of an ASV in the presence of model parametric uncertainties and external disturbances are stated in the following theorem.

Theorem 1: Consider the ASV dynamic model described by the kinematics (1) and the dynamics (2), and suppose that both Assumption 1 and condition (20) hold. Then, given a reference trajectory $\mathbf{p}_d(\gamma)$ of class at least $\mathcal{C}^2$, the control law (18) renders the origin of the error system $(\mathbf{z}_1(t), \mathbf{z}_2(t))$, given by (5) and (8), a global attractor in the presence of parametric uncertainty and constant external disturbances.

Proof: Start by recalling the Lyapunov function given by (11), and further recall its derivative, given by (12). According to the Property 2) of the projection operator (15), one has

$$-\tilde{\boldsymbol{\theta}}_{\mathbf{v}}^\mathsf{T}(t)\left[\boldsymbol{\Phi}_v^\mathsf{T}(\mathbf{v}, \mathbf{R})\mathbf{M}\mathbf{z}_2(t) + \Lambda_{\mathbf{v}}^{-1}\dot{\hat{\boldsymbol{\theta}}}_{\mathbf{v}}(t)\right] \leq 0$$

and

$$-\tilde{\boldsymbol{\theta}}_r^\mathsf{T}(t)\left[-\boldsymbol{\Phi}_r^\mathsf{T}(r)\boldsymbol{\delta}^\mathsf{T}\mathbf{S}\mathbf{M}\mathbf{z}_2(t) + \Lambda_r^{-1}\dot{\hat{\boldsymbol{\theta}}}_r(t)\right] \leq 0.$$

Moreover, based on Property 1), the results of the projection operator are bounded for all $t \geq 0$. Then, using the control law (18) and the bounded integral actions (16) and (17), it follows from (11) that

$$\frac{d}{dt}V_3(\tilde{\boldsymbol{\theta}}_{\mathbf{v}}, \tilde{\boldsymbol{\theta}}_r, \mathbf{z}_1, \mathbf{z}_2) = -Z_2(\mathbf{z}_1, \mathbf{z}_2)$$
$$= -k_1\|\sigma(\mathbf{z}_1)\|^2 - k_2\|\mathbf{z}_2\|^2.$$

We proceed now to calculate time-independent lower and upper bounds for V_3. Notice immediately that, by construction, $V_3(\tilde{\boldsymbol{\theta}}_{\mathbf{v}}, \tilde{\boldsymbol{\theta}}_r, \mathbf{z}_1, \mathbf{z}_2) \geq V_1(\mathbf{z}_1)$. Then, from (11), we have that

$$V_3(\tilde{\boldsymbol{\theta}}_{\mathbf{v}}, \tilde{\boldsymbol{\theta}}_r, \mathbf{z}_1, \mathbf{z}_2) \leq V_2(\mathbf{z}_1, \mathbf{z}_2) + \frac{\|\tilde{\boldsymbol{\theta}}_{\mathbf{v}}(t)\|^2}{2\min(\Lambda_{\mathbf{v}})} + \frac{\|\tilde{\boldsymbol{\theta}}_r(t)\|^2}{2\min(\Lambda_r)}.$$

According to Assumption 1 and to the Property 1) of the projector (15), it must be

$$\|\tilde{\boldsymbol{\theta}}_{\mathbf{v}}(t)\| \leq \|\boldsymbol{\theta}_{\mathbf{v}}(t)\| + \|\hat{\boldsymbol{\theta}}_{\mathbf{v}}(t)\| \leq \zeta_{\mathbf{v}} + \zeta_{\mathbf{v}} + \varepsilon = 2\zeta_{\mathbf{v}} + \varepsilon.$$

Likewise, $\|\tilde{\boldsymbol{\theta}}_r(t)\| \leq 2\zeta_r + \varepsilon$. This allows us to conclude that

$$V_3(\tilde{\boldsymbol{\theta}}_{\mathbf{v}}, \tilde{\boldsymbol{\theta}}_r, \mathbf{z}_1, \mathbf{z}_2) \leq V_2(\mathbf{z}_1, \mathbf{z}_2) + \frac{(2\zeta_{\mathbf{v}} + \varepsilon)^2}{2\min(\Lambda_{\mathbf{v}})} + \frac{(2\zeta_r + \varepsilon)^2}{2\min(\Lambda_r)}.$$

Consider now three auxiliary continuous positive definite functions defined as

$$W_1(\mathbf{z}_1) := V_1(\mathbf{z}_1),$$

$$W_2(\mathbf{z}_1, \mathbf{z}_2) := V_2(\mathbf{z}_1, \mathbf{z}_2) + \frac{(2\zeta_{\mathbf{v}} + \varepsilon)^2}{2\min(\Lambda_{\mathbf{v}})} + \frac{(2\zeta_r + \varepsilon)^2}{2\min(\Lambda_r)}, \text{ and}$$

$$W(\mathbf{z}_1, \mathbf{z}_2) := k_1\|\sigma(\mathbf{z}_1)\|^2 + k_2\|\mathbf{z}_2\|^2.$$

Therefore, we can write down the system of inequalities:

$$W_1(\mathbf{z}_1) \leq V_3(\tilde{\boldsymbol{\theta}}_{\mathbf{v}}, \tilde{\boldsymbol{\theta}}_r, \mathbf{z}_1, \mathbf{z}_2) \leq W_2(\mathbf{z}_1, \mathbf{z}_2)$$
$$\frac{d}{dt}V_3(\tilde{\boldsymbol{\theta}}_{\mathbf{v}}, \tilde{\boldsymbol{\theta}}_r, \mathbf{z}_1, \mathbf{z}_2) \leq -W(\mathbf{z}_1, \mathbf{z}_2).$$

Notice that $W_1(\mathbf{z}_1)$ is radially unbounded. Moreover, straightforward algebraic manipulations show that, for $(\mathbf{z}_1(t), \mathbf{z}_2(t)) =$

$\mathbf{0}$, the derivative of $\mathbf{z}_1(t)$ is identically zero, therefore bounded for all $t \geq 0$. In turn, we have, also for $(\mathbf{z}_1(t), \mathbf{z}_2(t)) = \mathbf{0}$, that

$$\dot{\mathbf{z}}_2(t) = -\mathbf{\Phi}_{\mathbf{v}}(\mathbf{v}, \mathbf{R})\tilde{\boldsymbol{\theta}}_{\mathbf{v}}(t) - \mathbf{S}\boldsymbol{\delta}\mathbf{\Phi}_r(r)\tilde{\boldsymbol{\theta}}_r(t),$$

where all variables involved are bounded[2]. We have thus laid down the necessary conditions to invoke [27, Theorem 8.4], which states that, under all the above outcomes, and for any pair $(\mathbf{z}_1(0), \mathbf{z}_2(0)) \in \mathbb{R}^4$, the error system $(\mathbf{z}_1(t), \mathbf{z}_2(t))$ is bounded and satisfies $W(\mathbf{z}_1, \mathbf{z}_2) \to 0 \,\text{as}\, t \to \infty$, which implies $\mathbf{z}_1 \to 0$ and $\mathbf{z}_2 \to 0$ as $t \to \infty$. This concludes the proof.[3] □

Remark 1: Theorem 1 proves that the system errors converge globally to zero, regardless of parametric uncertainties and exogenous disturbances, which are compensated by the integrators included in the control law. This robust strategy is markedly advantageous for systems which are difficult to identify rigorously, or for systems whose model may slightly change upon installing additional sensors or other devices, as is the case of marine robots. In case of time-varying external disturbances, the asymptotic stability guarantees give place to uniformly ultimately bounded errors.

Remark 2: There is nothing imposing the need for *a priori* information about the model parameters. In other words, our own approximations $\bar{\boldsymbol{\phi}}_{\mathbf{v}}$ and $\bar{\phi}_r$ can be zero, and so do the initial conditions of both (16) and (17), i.e., $\hat{\boldsymbol{\theta}}_{\mathbf{v}}(0)$ and $\hat{\phi}_r(0)$.

V. Zero Dynamics

The zero dynamics of a system can be interpreted as the resultant internal dynamics when suitable initial conditions and control inputs are applied to maintain the outputs zero for all time [28]. With this definition in mind, we understand how critical it is to investigate the stability of the zero dynamics when, in particular for this work, the controller (18) has driven the system error $(\mathbf{z}_1(t), \mathbf{z}_2(t))$ to zero.

The following analysis will provide us a deeper insight into the ASV's behavior.

A. Stability Analysis

Start by setting $\mathbf{z}_1(t)$ and $\mathbf{z}_2(t)$ to zero, which, according to (5) and (8), yields a kinematics subsystem whose equations are given by $\mathbf{p}(t) = \mathbf{p}_d(\gamma) - \mathbf{R}(t)\boldsymbol{\delta}$ and

$$\mathbf{v}(t) = \mathbf{R}^{\mathsf{T}}(t)\dot{\mathbf{p}}_d(\gamma) - r(t)\mathbf{S}\boldsymbol{\delta}. \tag{21}$$

Accordingly, $\mathbf{h}(t)$ in the control law (18) simplifies down to

$$\begin{aligned}\mathbf{h}(t) :=\ & r(t)\mathbf{S}\mathbf{M}\mathbf{v}(t) - \mathbf{M}\mathbf{S}\mathbf{R}^{\mathsf{T}}(t)\dot{\mathbf{p}}_d(\gamma)r(t) + \mathbf{M}\mathbf{R}^{\mathsf{T}}(t)\ddot{\mathbf{p}}_d(\gamma) \\ & + \mathbf{M}\mathbf{\Phi}_{\mathbf{v}}(\mathbf{v}, \mathbf{R})\left(\bar{\boldsymbol{\phi}}_{\mathbf{v}} + \hat{\boldsymbol{\theta}}^*_{\mathbf{v}}\right) + \mathbf{M}\mathbf{S}\boldsymbol{\delta}\mathbf{\Phi}_r(r)\left(\bar{\phi}_r + \hat{\theta}^*_r\right),\end{aligned} \tag{22}$$

where $\hat{\boldsymbol{\theta}}^*_{\mathbf{v}}$ and $\hat{\theta}^*_r$ are auxiliary variables holding the steady-state values of the integral action (16) and (17), respectively[4]. Finally, the ASV's zero dynamics angular velocity is governed by the following differential equation:

$$\dot{r}(t) = -\frac{\ell}{J - (m - Y_{\dot{v}})\delta_x \ell}\mathbf{u}_2^{\mathsf{T}}\mathbf{h}(t) - \mathbf{\Phi}_r(r)\boldsymbol{\phi}_r. \tag{23}$$

Notice that, under the condition in (20), (23) is always well-defined. Expressing (21) component-wise, given $\mathbf{v}(t) = [u(t), v(t)]^{\mathsf{T}}$ and recalling that $\boldsymbol{\delta} = [\delta_x, 0]^{\mathsf{T}}$, results in

$$\begin{cases} u(t) = \mathbf{u}_1^{\mathsf{T}}\mathbf{R}^{\mathsf{T}}(t)\dot{\mathbf{p}}_d(\gamma) \\ v(t) = v_d(t) - r(t)\delta_x \end{cases}, \tag{24}$$

where $v_d(t) := \mathbf{u}_2^{\mathsf{T}}\mathbf{R}^{\mathsf{T}}(t)\dot{\mathbf{p}}_d(\gamma)$. As $\dot{\mathbf{p}}_d(\gamma)$ is bounded for all $t \geq 0$, it follows that $u(t)$ and $v_d(t)$ are bounded for all $t \geq 0$ as well. It remains to be checked the boundedness of both the sway motion $v(t)$ and the angular velocity $r(t)$.

Take the derivative of $v(t)$, written as

$$\dot{v}(t) = -\frac{u(t)v_d(t)}{\delta_x} + \frac{u(t)v(t)}{\delta_x} + \mathbf{u}_2^{\mathsf{T}}\mathbf{R}^{\mathsf{T}}(t)\ddot{\mathbf{p}}_d(\gamma) - \dot{r}(t)\delta_x. \tag{25}$$

From (23), and based on (4), we can write

$$\begin{aligned}\dot{r}(t)\delta_x = \beta\mathbf{u}_2^{\mathsf{T}}\mathbf{h}(t)\delta_x - \frac{d_r}{J}(v_d(t) - v(t)) + \frac{b_r\delta_x}{J} \\ - \frac{d_{r|r|}}{J\delta_x}(v_d(t) - v(t))|v_d(t) - v(t)|,\end{aligned} \tag{26}$$

with $\beta := -\ell/(J - (m - Y_{\dot{v}})\delta_x\ell)$. Next, long but straightforward algebraic manipulations allow us to write, based on (22),

$$\begin{aligned}\mathbf{u}_2^{\mathsf{T}}\mathbf{h}(t) =\ & \mathbf{u}_2^{\mathsf{T}}\mathbf{M}\mathbf{R}^{\mathsf{T}}(t)\ddot{\mathbf{p}}_d(\gamma) - \mathbf{u}_2^{\mathsf{T}}\mathbf{R}^{\mathsf{T}}(t)^I\mathbf{b}^*_{\mathbf{v}} - \frac{\delta_x(m - Y_{\dot{v}})b^*_r}{J} \\ & + \left[\frac{u(t)(Y_{\dot{v}} - X_{\dot{u}})}{\delta_x} + \frac{(m - Y_{\dot{v}})d^*_r}{J}\right](v_d(t) - v(t)) + \mathbf{u}_2^{\mathsf{T}}\mathbf{d}^*_l v(t) \\ & + \frac{(m - Y_{\dot{v}})d^*_{r|r|}}{J\delta_x}(v_d(t) - v(t))|v_d(t) - v(t)| + \mathbf{u}_2^{\mathsf{T}}\mathbf{d}^*_q v(t)|v(t)|,\end{aligned} \tag{27}$$

where the terms with superscript $(\cdot)^*$ correspond to the respective steady-state values associated with the integral actions (16) and (17). Substituting (27) and (26) in (25) yields

$$\begin{aligned}\dot{v}(t) =\ & \alpha_0(t) + \alpha_v(t)v(t) - \beta\delta_x\mathbf{u}_2^{\mathsf{T}}\mathbf{d}^*_q v(t)|v(t)| \\ & + \left(\frac{d_{r|r|}}{\delta_x J} - \frac{\beta(m - Y_{\dot{v}})d^*_{r|r|}}{J}\right) \\ & \times (v_d(t) - v(t))|v_d(t) - v(t)|,\end{aligned} \tag{28}$$

where $\alpha_0(t) \in \mathbb{R}$ is the coefficient of degree zero, with respect to $v(t)$, defined as

$$\alpha_0(t) := -\frac{u(t)v_d(t)}{\delta_x} + \mathbf{u}_2^{\mathsf{T}}\mathbf{R}^{\mathsf{T}}(t)\ddot{\mathbf{p}}_d(\gamma) - \frac{b_r\delta_x}{J} + \frac{d_r}{J}v_d(t)$$

[2]Please refer to Section V for a rigorous proof of this claim.

[3]An alternative proof of Theorem 1 can be done resorting directly to Barbalat's lemma. We preferred this approach for the sake of simplicity, in the sense that we avoid having to compute the second derivative of $V_3(t, \mathbf{z}_1, \mathbf{z}_2)$ to show that $\dot{V}_3(t, \mathbf{z}_1, \mathbf{z}_2)$ is uniformly continuous.

[4]Note that, because $\mathbf{z}_1(t)$ and $\mathbf{z}_2(t)$ are zero, $\dot{\hat{\boldsymbol{\theta}}}_{\mathbf{v}}(t)$ and $\dot{\hat{\boldsymbol{\theta}}}_r(t)$, as given by (16) and (17), are also zero.

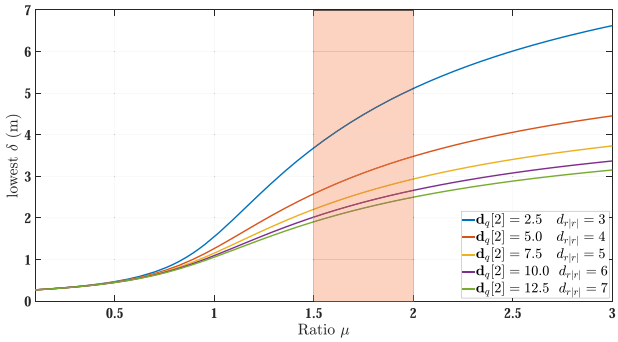

Fig. 3. Relationship between lowest δ_x and ratio μ.

$$- \beta\delta_x \left\{ \mathbf{u}_2^{\mathsf{T}} \mathbf{M} \mathbf{R}^{\mathsf{T}}(t) \left[\ddot{\mathbf{p}}_d(\gamma) - {}^{I}\mathbf{b}_{\mathbf{v}}^{*} \right] + \frac{(m - Y_{\dot{v}})}{J} \left[d_r^* v_d(t) - \delta_x b_r^* \right] \right\} - \beta u(t)(Y_{\dot{v}} - X_{\dot{u}}) v_d(t),$$

and where $\alpha_v(t) \in \mathbb{R}$ is the coefficient of degree 1, with respect to $v(t)$, defined as

$$\alpha_v(t) := \frac{u(t)}{\delta_x} - \frac{d_r}{J} - \beta\delta_x \left[\mathbf{u}_2^{\mathsf{T}} \mathbf{d}_l^* - \frac{(m - Y_{\dot{v}}) d_r^*}{J} - \frac{u(t)(Y_{\dot{v}} - X_{\dot{u}})}{\delta_x} \right].$$

In order for $v(t)$ to be bounded, the coefficient in the dominant term in (28), i.e., $v(t)|v(t)|$, should be negative. Following some algebraic manipulations, we shall thus guarantee that

$$\frac{\ell J \mathbf{u}_2^{\mathsf{T}} \mathbf{d}_q^* \delta_x^2 - (m - Y_{\dot{v}}) \ell (d_{r|r|}^* - d_{r|r|}) \delta_x - J d_{r|r|}}{J\delta_x \left[J - (m - Y_{\dot{v}}) \ell \delta_x \right]} < 0. \quad (29)$$

The inequality in (29) is satisfied for a positive numerator and negative denominator, and vice versa. Since $\delta_x > 0$, the case when the denominator is positive and the numerator is negative leads to very small values for δ_x, less than a few centimeters, which causes the system to perform poorly.

For positive numerator and negative denominator, we start by noting that, typically, $\mathbf{d}_q^*$ and $d_{r|r|}^*$ do not converge to the bound; they will settle close to the actual values. Hence, for analysis purposes only, suppose that $\mathbf{d}_q^* = \mu \mathbf{d}_q$ and $d_{r|r|}^* = \mu d_{r|r|}$, for some $\mu > 0$. Empirical evidence and extensive simulations suggest that worst-case values for μ lie in the region between 1.5 and 2, which corresponds to an overcompensating integral action. By selecting $\mu \in [1.5, 2]$, we can then compute a conservative lower bound for δ_x in function of μ that satisfies (29). The results are displayed in Fig. 3, given different values of $\mathbf{u}_2^{\mathsf{T}} \mathbf{d}_q$ and $d_{r|r|}$; other physical constants are identical to the ones listed in Table I. Ultimately, we set $\delta_x > 2$ m.

Finally, with $v(t)$ bounded, we conclude from (24) that $r(t)$ is also bounded. Therefore, with condition (29) holding, in particular, for $\delta_x > 2$ m, the system's zero dynamics is stable.

TABLE I
ASV PHYSICAL PARAMETERS

Parameter	Value	SI Units
$m,\ X_{\dot{u}},\ Y_{\dot{v}}$	$20,\ -1.0,\ -3.9270$	kg
J	2.9434	kg·m^2
$\mathbf{d}_l$	$[10,\ 25]^{\mathsf{T}}$	kg/s
$\mathbf{d}_q$	$[7,\ 11]^{\mathsf{T}}$	kg/m
d_r	20	kg·m^2/s
$d_{r\|r\|}$	5	kg·m

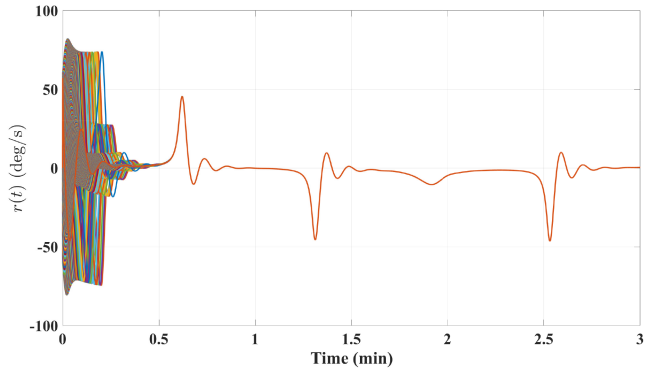

Fig. 4. Time evolution of $r(t)$ sequences.

B. Monte Carlo Simulation

The equations in (21) and (23) describe the motion of the ASV when the system errors remain identically zero. In the previous analysis, we have ascertained that, when errors are zero, the dynamics in (23) is stable, which guarantees boundedness of $\mathbf{v}(t)$ and, therefore, boundedness of all system variables.

We shall now resort to the Monte Carlo method to illustrate what happens to $r(t)$ under different initial conditions for $\psi(0)$ and $r(0)$. At the same time, we will confirm that there are no error *leakages*, i.e., that $\mathbf{z}_1(t)$ and $\mathbf{z}_2(t)$ indeed remain zero for all time, as suggested by Theorem 1.

Our Monte Carlo, implemented in MATLAB, considers $\psi(0)$ ranging in the interval $[-180, 180]$ (deg) with steps of 2 degrees, and $r(0)$ ranging in the interval $[-60, 60]$ (deg/s) with steps of 2 degrees per second. This results in 11041 simulation runs. Each simulation is then carried out for 3 minutes. The details of the Monte Carlo simulation, including the desired trajectory, and ASV physical model, are identical to the ones reported in Section VI-B.

Fig. 4 displays the time evolution of the 11041 sequences of $r(t)$. After roughly around 30 seconds, all sequences have converged into a single one. This confirms the absence of erratic behaviors in the zero dynamics, which corroborates the claim that (23) is stable.

To further confirm that both $\mathbf{z}_1(t)$ and $\mathbf{z}_2(t)$ remain identically zero for all $t \geq 0$, we can compute their corresponding maximum values for each of the 11041 Monte Carlo runs and then verify that these maxima are zero within the tolerances of the ODE solver and unavoidable numerical errors due to the use of floating point numbers. Figs. 5 and 6 display the maximum values of $\mathbf{z}_1$ and $\mathbf{z}_2$ against each respective pair of initial conditions

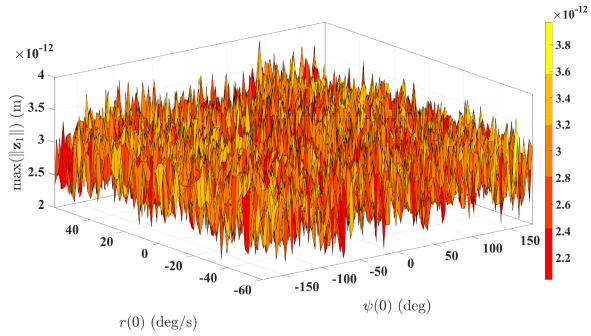

Fig. 5. Maximum value of $\|\mathbf{z}_1\|$.

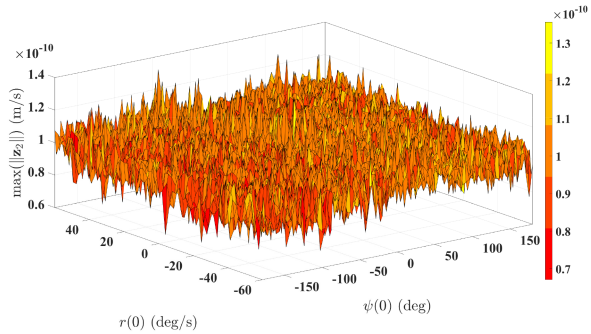

Fig. 6. Maximum value of $\|\mathbf{z}_2\|$.

$(\psi(0), r(0))$. From the surface plots we conclude that the magnitude of the errors remain below 4×10^{-12} for $\mathbf{z}_1$ and below 1.4×10^{-10} for $\mathbf{z}_2$, for all $t \geq 0$, which is in accordance with the statement of Theorem 1.

VI. Computer Simulation of Path Following Control

A. Speed Profile

The development of a desired speed profile $\dot{\gamma}(t)$ is now presented as a preparation for the simulations and experiments.

Define a bump function $\Psi : \mathbb{R} \to \mathbb{R}$, smooth, of class $\mathcal{C}^\infty$, and of compact support, as

$$\Psi(s) := \begin{cases} 1, & |s| < \xi_1 \\ \frac{1}{2}\tanh\left(-\frac{\lambda(|s|)}{1-\lambda^2(|s|)}\right) + \frac{1}{2}, & \xi_1 \leq |s| < \xi_2 \\ 0, & \xi_2 \leq |s| \end{cases},$$

where $\lambda(|s|) = \frac{2|s|-(\xi_1+\xi_2)}{\xi_2-\xi_1}$, with $\xi_2 > \xi_1 > 0$. We then define the desired speed profile in function of the position error as

$$\dot{\gamma}(t) := V_d(t)\Psi\left(\|\mathbf{z}_1(t)\|\right), \tag{30}$$

where $V_d(t)$ is a function designed to meet certain control requirements, e.g., a constant speed profile.

B. Setup

Consider a reference trajectory in the form of a Lissajous curve, with ratio $3/2$ and phase angle $\pi/2$, described by the following parametric position vector:

$$\mathbf{p}_d(\gamma) = 30\left[\sin\left(3\gamma(t) + \tfrac{\pi}{2}\right), \quad \sin\left(2\gamma(t)\right)\right]^\mathsf{T} \text{ (m)}, \tag{31}$$

with $\gamma(t) \in \mathbb{R}$ computed from (30), and where

$$V_d(t) := 2\left\|\frac{\partial \mathbf{p}_d(\gamma)}{\partial \gamma}\right\|^{-1}. \tag{32}$$

Note that by choosing this type of curve we ensure the reference speed to be constant, more specifically, $\|\dot{\mathbf{p}}_d(\gamma)\| = 2\,\text{m/s}$ for all $t \geq 0$.

A comparison study was carried out between the proposed methodology and four other different but related strategies, including a conventional backstepping approach and the three methodologies reported in [4], [7] and [9]. For this study, the external disturbances are characterized by a Brownian motion governed by the following differential equations: ${}^I\dot{\mathbf{b}}_\mathbf{v}(t) = [-{}^I\mathbf{b}_\mathbf{v}(t) + 1200\mathbf{w}_{{}^I\mathbf{b}_\mathbf{v}}(t)]/10$, and $\dot{b}_r(t) = [-b_r(t) + 600\mathbf{w}_{b_r}(t)]/10$, where $\mathbf{w}_{{}^I\mathbf{b}_\mathbf{v}} \in \mathbb{R}^2$ and $\mathbf{w}_{b_r} \in \mathbb{R}$ correspond to zero-mean white Gaussian noise sequences. In another study, solely conducted for validation purposes, the values of the disturbances were set, in view of (2), to ${}^I\mathbf{b}_\mathbf{v} = [3.33,\ 6.66]^\mathsf{T}$ (N) and $b_r = -0.08\,(\text{N}\cdot\text{m})$.

The vehicle's constant physical parameters that were employed in the simulations are shown in Table I. The variables corresponding to the partly known information were set to $\bar{\boldsymbol{\phi}}_\mathbf{v} = [0.6\mathbf{d}_l^\mathsf{T}, 0.55\mathbf{d}_q^\mathsf{T}, \mathbf{0}]^\mathsf{T}$ and $\bar{\boldsymbol{\phi}}_r = [0.75d_r, 0.8d_{r|r|}, 0]^\mathsf{T}$ in both studies. These represent an underestimation of the model parameters and a total lack of knowledge regarding the disturbances. In turn, the initial values of the integral terms expressed by (16) and (17) were set to $\hat{\boldsymbol{\theta}}_\mathbf{v}(0) = [0.06\mathbf{d}_l^\mathsf{T}, 0.055\mathbf{d}_q^\mathsf{T}, \mathbf{0}]^\mathsf{T}$ and $\hat{\boldsymbol{\theta}}_r(0) = [0.075d_r, 0.08d_{r|r|}, 0]^\mathsf{T}$, respectively. The initial position of the vessel was set to $\mathbf{p}(0) = [32, -2]^\mathsf{T}$ m and the initial orientation to $\psi(0) = 0$ degrees.

The list of gains used in the simulations is shown in Table II. Regarding the bump function in (30), we set $\xi_2 = 10$ m and $\xi_1 = 3$ m.

The controller, including the integral effect, and the ASV's dynamic model were implemented in a continuous-time framework using the Runge-Kutta method with a variable time step. The solutions of all the differential equations involved were obtained using the MATLAB solver ode45 for a time span of 5 minutes.

Remark 3: The gains $\Lambda_\mathbf{v}$ and Λ_r affect primarily the convergence time of the integral actions in (16) and (17); they should be kept lower in practice to avoid abrupt, potentially destabilizing, maneuvers of the vessel. The gain $\kappa_{\max}$ adjusts the limits of the saturation function (7). Finally, the gains k_1 and k_2 affect the convergence of the position and velocity errors. In practice,

TABLE II
Control Gains Used in the Simulations

Parameter	Value
Λ_v	diag(3, 3, 4, 4, 5, 5)
Λ_r	diag(3, 4, 5)
$\kappa_{\max},\ k_1,\ k_2$	0.1, 15, 10
$\boldsymbol{\delta}$	$[3.5,\ 0]^\mathsf{T}$

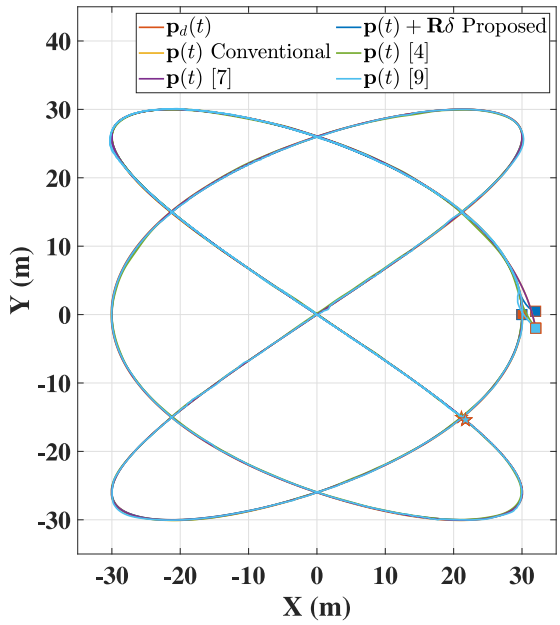

Fig. 7. Top view of desired and actual trajectories. Squares and stars mark the start and end points, respectively, of each trajectory.

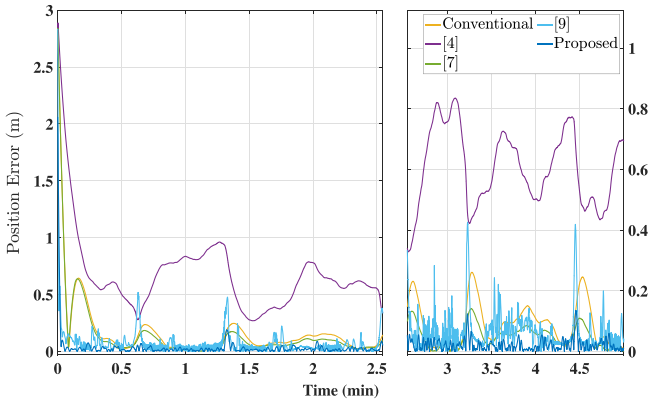

Fig. 8. Comparison study: norm-evolution of the position error. Zoom in view shown on right subplot.

these last three scalar gains should be higher than in simulation to compensate for the slower evolution of the integral actions, but not to high in order to avoid saturation of the actuators.

C. Simulation Results

Fig. 7 displays the desired and actual trajectories of the comparison study. Notice that this maneuver is quite demanding in terms of torque actuation, especially because describing sharp turns at constant speed require large angular velocities, and subjects the vessel to large centrifugal forces.

Fig. 8 shows the norm-evolution of position error for the five methodologies. The controller proposed in [4] was not designed to tackle external disturbances. Therefore, as expected, this controller is the worse among the batch, ultimately serving the purpose of demonstrating how crucial it is to always address

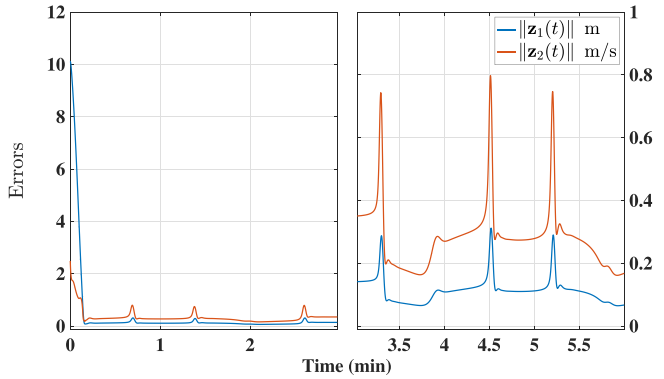

Fig. 9. Evolution of the error variables in a scenario without integral action. Zoom in view shown on right subplot.

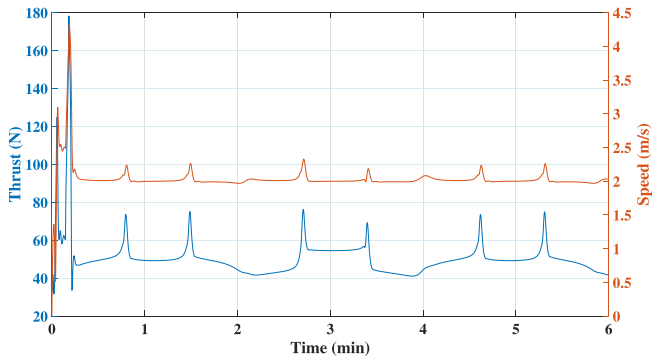

Fig. 10. Thrust actuation vs. speed profile.

external disturbance rejection in control of autonomous vehicles. The work reported in [9] assumes that the hydrodynamic damping is linear, which is not the case for the model presented above, also resulting in poorer performance. The reference trajectory, in view of its constant speed profile, is quite demanding, especially during the sharp turns, where all controllers struggle to maintain the desired constant speed while performing the maneuver, resulting in a sudden increase of the position error. This effect can be seen in Fig. 8 at the 0.6, 1.4, 2.5, 3.2, and 4.4 minute marks. The proposed controller is consistently the one with lower position error both in the straight sections and in the tight curves.

Fig. 9 showcases individual resulting errors when the integral action of the proposed controller is switched off, in a scenario with constant disturbances and larger initial position error. We doubled the values of k_1 and k_2 in order to alleviate the steep drop in performance, thus making the comparison fairer. Still, the position error is approximately one order of magnitude larger than its counterpart illustrated in Fig. 8. If we continued increasing k_1 and k_2, we would see slightly smaller errors (although never as small as those attained with integral action), at the expense of an increasingly higher thrust force actuation, eventually defying the ASV's physical limitations.

Figs. 10 through 13 correspond to validation simulation results of the proposed method in a scenario with constant external disturbances. Fig. 10 showcases the combined thrust produced

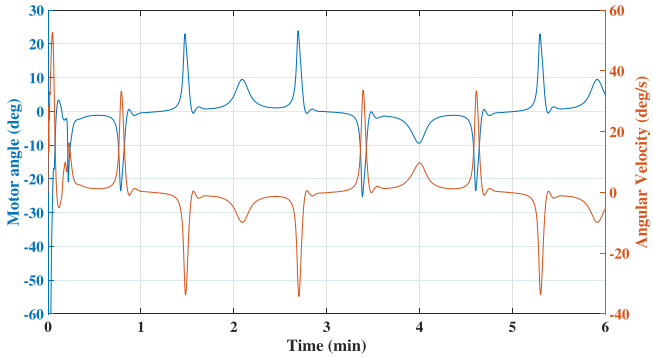

Fig. 11. Motor angle $\theta(t)$ vs. angular velocity $r(t)$.

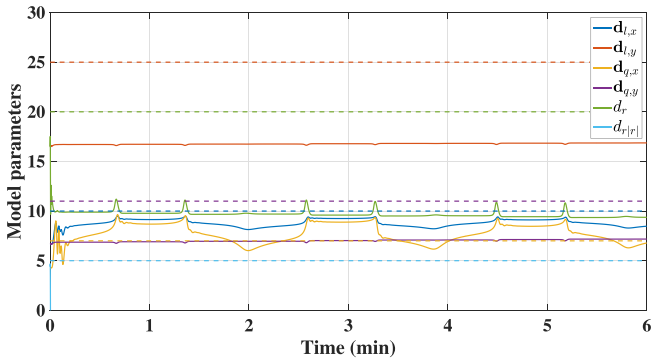

Fig. 12. Integral compensation for model parametric uncertainty.

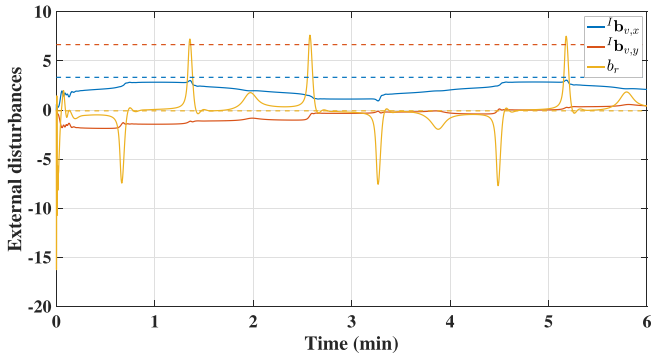

Fig. 13. Integral compensation for external disturbances.

by the motors along with the resulting speed profile. One can observe bumps and small variations in thrust, which are a consequence of the ASV trying to counteract the influence of the exogenous disturbances, as well as performing sharp turns. The controller is nonetheless able to maintain for the most part a practically constant speed of 2 m/s, as per design requirement.

The motor angle $\phi(t)$ is displayed in Fig. 11 along with the evolution of the ASV's angular velocity.

Finally, the plots in Figs. 12 and 13 illustrate the evolution of the integral compensation associated with the model parametric uncertainty and the external disturbances, respectively. In both figures, the dashed lines indicate, for reference only, the corresponding actual constant values.

Fig. 14. Surface vessel Q-Boat 1800P used for operations on a lake at the University of Macau.

Fig. 15. Surface vessel Q-Boat 1800P motors.

VII. Lake Trials Using an Autonomous Surface Vehicle

A. The Testbed

The final instrumented ASV used in the experiments is shown in Fig. 14. For a full account of the experimental setup, please refer to [25].

The ASV motors, which are shown in Fig. 15, are current-controlled DC-motors with a maximum angle of ± 60 degrees, and can produce a combined thrust of up to 200 N.

The model parameters used in the experiments are identical to the ones listed in Table I.

B. Experimental Results

The Q-Boat ASV was programmed to describe a parameterized curve identical to the curve outlined by equations (31) and (32). The overall sampling rate in the experiments was set to 50 Hz. The 4th order Runge–Kutta method was employed to compute the solutions of the integral actions.

Table III lists the control gains, which were empirically tuned for the best performance.

Fig. 16 displays the desired and actual trajectories. Notice that, for the entirety of the maneuver, the vehicle remains very close to the desired position. This is further confirmed by the steady-state mean and standard deviation of the position error, computed for

TABLE III
CONTROL GAINS USED IN THE EXPERIMENTS

Parameter	Value
Λ_v	$10^{-3}\,\mathrm{diag}(1,3,.5,4,5,3)$
Λ_r	$10^{-3}\,\mathrm{diag}(1,1,1)$
$\kappa_{\max},\ k_1,\ k_2$	$4,\ 60,\ 60$
$\boldsymbol{\delta}$	$[3.5,\ 0]^{\mathsf{T}}$

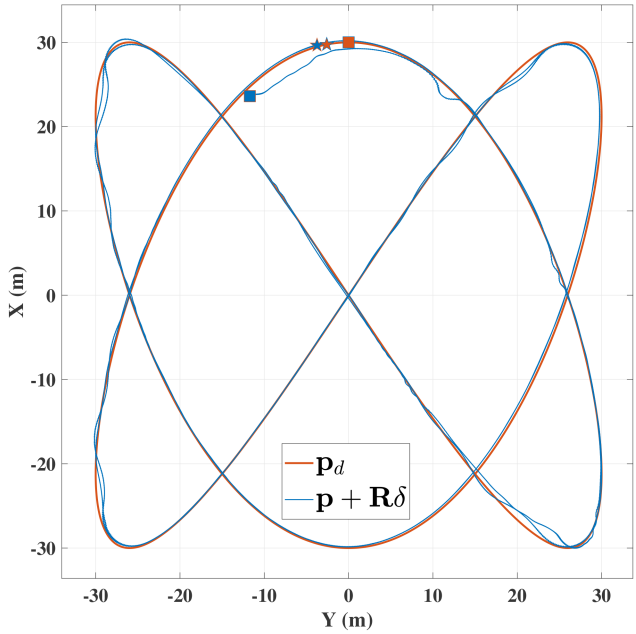

Fig. 16. Top view of desired and actual trajectories. Squares and stars mark the start and end points, respectively, of each trajectory.

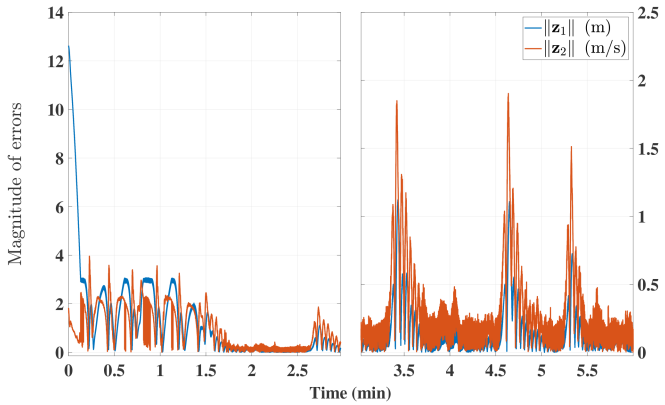

Fig. 17. Evolution of the error variables. Zoom in view shown on right subplot.

$t \geq 180$ seconds, of around 16.62 cm and 12.62 mm, respectively, which attests the good performance of the path following control application.

In all remaining figures, the transient period is noticeable for around 1.5 minutes. During this time, the controller is more reactive due to integral action more volatile in nature.

Fig. 17 shows simultaneously the norm-evolution of the two error variables $\mathbf{z}_1(t)$ and $\mathbf{z}_2(t)$. Similar to the simulations, here $\mathbf{z}_2(t)$ is also relatively larger than $\mathbf{z}_1(t)$. It's important to recall

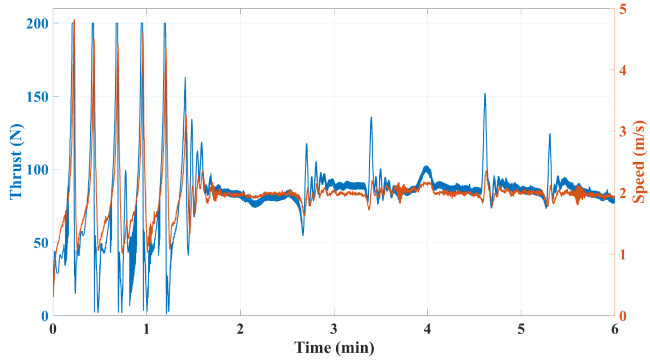

Fig. 18. Thrust actuation vs. speed profile.

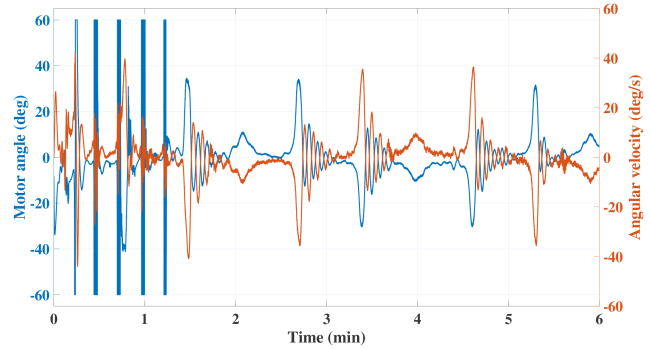

Fig. 19. Motor angle vs. angular velocity.

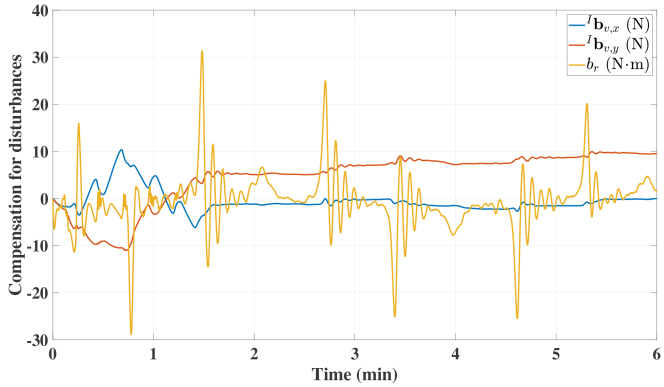

Fig. 20. Integral action compensation for exogenous disturbances.

that $\mathbf{z}_2(t)$, by definition (8), has a term which is proportional to $\sigma(\mathbf{z}_1)$, which causes these larger deviations.

Fig. 18 showcases the combined thrust produced by the motors along with the resulting speed profile. Once again, the small variations in thrust are a consequence of the ASV trying to perform the sharp turns and counteracting the influence of the exogenous disturbances. This notwithstanding, the controller in the experiments is also able to maintain for the most part a practically constant speed of 2 (m/s).

In turn, the motor angle is displayed in Fig. 19 along with the evolution of the ASV's angular velocity.

The evolution of the compensation for exogenous disturbances is shown in Fig. 20. We emphasize that this compensation

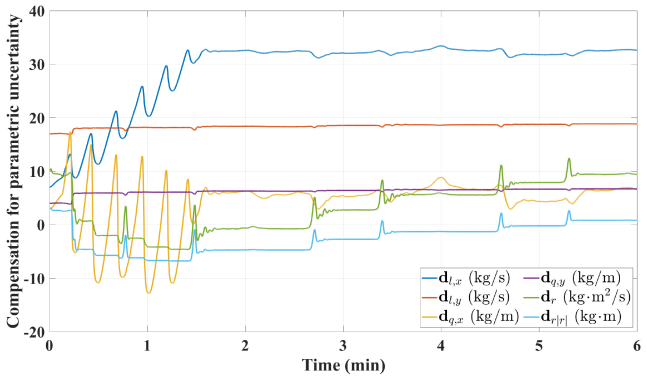

Fig. 21. Integral action compensation for model parametric uncertainty: linear and angular hydrodynamic damping terms.

does not represent an estimation. The compensation is the result of an integral action. Nevertheless, it's particularly obvious that the ASV's linear an angular motion is affected by existing exogenous disturbances, which, as witnessed during the trials, were caused by a constant and significant wind flow, generating small waves, as well as by lake currents.

Finally, the evolution of the compensations for linear and angular hydrodynamic damping terms is shown in Fig. 21.

We emphasize that, according to (18), as well as to the properties of projector (15), and in light of the zero dynamics analysis carried out in Section V, the actuation is theoretically bounded. By tweaking of the control gains, specifically the ones listed in Table III, we can make sure the magnitude of the thrust and torque remains below some predetermined values.

VIII. Conclusion

This paper presented the development of a stabilizing control law, bounded with respect to the position error, for the problem of path following of an ASV in the presence of model parametric uncertainty and exogenous disturbances. The proposed controller includes integral action to counteract the influence of the disturbances and parametric uncertainty. The origin of the resulting error system was shown to be a global attractor, and the performance of the controller was validated in simulation. The stability of the zero dynamics was theoretically addressed and extensively inspected resorting to a Monte Carlo analysis. Finally, we used an instrumented fully autonomous surface vehicle in a lake to showcase the performance achieved by the controller. The results confirm that our strategy is indeed advantageous for systems which are difficult to identify in a rigorous manner, as is the case of marine crafts. By using this controller, preliminary, expensive and often tedious model identification stages can, to some extent, be disregarded. Future work will focus on different control strategies, for example, nonlinear model predictive control, that may be combined with partial state estimators.

References

[1] J. Alves et al., "Vehicle and mission control of the DELFIM autonomous surface craft," in *Proc. 14th Mediterranean Conf. Control Automat.*, 2006, pp. 1–6.

[2] J. E. Manley, "Unmanned surface vehicles, 15 years of development," in *Proc. IEEE Oceans MTS Quebec Conf. and Exhib.*, 2008, pp. 1–4.

[3] F. Zhang, G. Marani, R. N. Smith, and H. T. Choi, "Future trends in marine robotics [TC spotlight]," *IEEE Robot. Automat. Mag.*, vol. 22, no. 1, pp. 14–122, Mar. 2015.

[4] A. P. Aguiar and J. P. Hespanha, "Trajectory-tracking and path-following of underactuated autonomous vehicles with parametric modeling uncertainty," *IEEE Trans. Autom. Control*, vol. 52, no. 8, pp. 1362–1379, Aug. 2007.

[5] M. Bibuli, G. Bruzzone, M. Caccia, and L. Lapierre, "Path-following algorithms and experiments for an unmanned surface vehicle," *J. Field Robot.*, vol. 26, no. 8, pp. 669–688, Aug. 2009.

[6] A. J. Sørensen, "A survey of dynamic positioning control systems," *Annu. Rev. Control*, vol. 35, no. 1, pp. 123–136, Apr. 2011.

[7] S. Yin and B. Xiao, "Tracking control of surface ships with disturbance and uncertainties rejection capability," *IEEE/ASME Trans. Mechatron.*, vol. 22, no. 3, pp. 1154–1162, Jun. 2017.

[8] N. Wang, H. R. Karimi, H. Li, and S.-F. Su, "Accurate trajectory tracking of disturbed surface vehicles: A finite-time control approach," *IEEE/ASME Trans. Mechatron.*, vol. 24, no. 3, pp. 1064–1074, Jun. 2019.

[9] C. Paliotta, E. Lefeber, K. Y. Pettersen, J. Pinto, M. Costa, and J. B. de Sousa, "Trajectory tracking and path following for underactuated marine vehicles," *IEEE Trans. Control Syst. Technol.*, vol. 27, no. 4, pp. 1423–1437, Jul. 2019.

[10] A. M. Lekkas and T. I. Fossen, "Integral LOS path following for curved paths based on a monotone cubic hermite spline parametrization," *IEEE Trans. Control Syst. Technol.*, vol. 22, no. 6, pp. 2287–2301, Nov. 2014.

[11] T. I. Fossen and A. M. Lekkas, "Direct and indirect adaptive integral line-of-sight path-following controllers for marine craft exposed to ocean currents," *Int. J. Adaptive Control Signal Process.*, vol. 31, no. 4, pp. 445–463, Mar. 2015.

[12] D. Belleter, M. A. Maghenem, C. Paliotta, and K. Y. Pettersen, "Observer based path following for underactuated marine vessels in the presence of ocean currents: A global approach," *Automatica*, vol. 100, pp. 123–134, Feb. 2019.

[13] K. D. Do and J. Pan, "Underactuated ships follow smooth paths with integral actions and without velocity measurements for feedback: Theory and experiments," *IEEE Trans. Control Syst. Technol.*, vol. 14, no. 2, pp. 308–322, Mar. 2006.

[14] Y. Li, Y. Liu, and S. Tong, "Observer-based neuro-adaptive optimized control of strict-feedback nonlinear systems with state constraints," *IEEE Trans. Neural Netw. Learn. Syst.*, vol. 33, no. 7, pp. 3131–3145, Jul. 2022.

[15] Y. Li, Y. Fan, K. Li, W. Liu, and S. Tong, "Adaptive optimized backstepping control-based RL algorithm for stochastic nonlinear systems with state constraints and its application," *IEEE Trans. Cybern.*, vol. 52, no. 10, pp. 10542–10555, Oct. 2022.

[16] Z. Zheng, "Moving path following control for a surface vessel with error constraint," *Automatica*, vol. 118, Aug. 2020, Art. no. 109040.

[17] F. Valenciaga, "A second order sliding mode path following control for autonomous surface vessels," *Asian J. Control*, vol. 16, no. 5, pp. 1515–1521, Feb. 2014.

[18] T. I. Fossen. *Handbook of Marine Craft Hydrodynamics and Motion Control*. Hoboken, NJ, USA: Wiley, 2011, pp. 45–58.

[19] G. Hitz, F. Pomerleau, F. Colas, and R. Siegwart, "Relaxing the planar assumption: 3D state estimation for an autonomous surface vessel," *Int. J. Robot. Res.*, vol. 34, no. 13, pp. 1604–1621, Jul. 2015.

[20] H. Xu and C. G. Soares, "Vector field path following for surface marine vessel and parameter identification based on," *LS-SVM. Ocean Eng.*, vol. 113 pp. 151–161, Feb. 2016.

[21] Y. Zhang, S. Li, and X. Liu, "Adaptive near-optimal control of uncertain systems with application to underactuated surface vessels," *IEEE Trans. Control Syst. Technol.*, vol. 26, no. 4, pp. 1204–1218, Jul. 2018.

[22] Z. Zheng and L. Sun, "Path following control for marine surface vessel with uncertainties and input saturation," *Neurocomputing*, vol. 177, pp. 158–167, Feb. 2016.

[23] G. Zhang and X. Zhang, "Concise robust adaptive path-following control of underactuated ships using DSC and MLP," *IEEE J. Ocean. Eng.*, vol. 39, no. 4, pp. 685–694, Oct. 2014.

[24] Z. Bell, A. Parikh, J. Nezvadovitz, and W. E. Dixon, "Adaptive control of a surface marine craft with parameter identification using integral concurrent learning," in *Proc. IEEE 55th Conf. Decis. Control.*, 2016, pp. 389–394.

[25] W. Xie, J. Reis, D. Cabecinhas, and C. Silvestre, "Design and experimental validation of a nonlinear controller for underactuated surface vessels," *Nonlinear Dyn.*, vol. 102, no. 4, pp. 2563–2581, Nov. 2020.
[26] Z. Cai, M. S. de Queiroz, and M. S. Dawson, "A sufficiently smooth projection operator," *IEEE Trans. Autom. Control*, vol. 51, no. 1, pp. 135–139, Jan. 2006.
[27] H. Khalil. *Nonlinear Systems. Pearson Education*, 3rd ed. Upper Saddle River, Hoboken, NJ, USA: Prentice Hall, ,2002.
[28] S. Y. Huang and K. Youcef-Toumi, "Zero Dynamics of Nonlinear MIMO Systems From System Configurations - A. Bond Graph Approach," *Proc. IFAC Proc. Vol.*, vol. 29 no. 1 pp. 4392–4397, Jun. 1996.

Joel Reis received the M.Sc. degree in aerospace engineering from Instituto Superior Técnico, Lisbon, Portugal, in 2013, and the Ph.D. degree in electrical and computer engineering from the University of Macau, Macau, in 2019. He is currently a Postdoctoral Fellow with the Faculty of Science and Technology, University of Macau. His research interests include estimation and control theory for autonomous vehicles.

Wei Xie (Member, IEEE) received the M.Sc. degree in electromechanical engineering and the Ph.D. degree in electrical and computer engineering from the University of Macau, Macau, in 2016 and 2021, respectively. He is currently an Assistant Professor with the Department of Automation, Shanghai Jiao Tong University, Shanghai, China. His research interests include nonlinear control of marine and aerial vehicles and coordinated control of multi-vehicle systems.

David Cabecinhas received the Licenciatura and Ph.D. degrees in electrical and computer engineering from the Instituto Superior Técnico, Universidade de Lisboa, Lisbon, Portugal, in 2006 and 2014, respectively. He is currently a Researcher with the Laboratory for Robotics and Engineering Systems, Institute for Systems and Robotics, Lisbon. His research interests include nonlinear control, sensor-based and vision-based control, modeling and identification, and fault detection and mitigation with applications to autonomous aerial, surface, and underwater robotic vehicles.

Carlos Silvestre (Senior Member, IEEE) received the Licenciatura degree in electrical engineering from the Instituto Superior Técnico (IST) of Lisbon, Portugal, in 1987, the master's degree in electrical engineering in 1991, and the Ph.D. degree in control science in 2000,and the the Habilitation degree in electrical engineering and computers from IST in 2011. Since 2000, he has been with the Department of Electrical Engineering of the Instituto Superior Técnico, where he is currently on leave. Since 2015, he has been with the Faculty of Science and Technology of the University of Macau, Macau, where he currently holds a Professor position with the Department of Electrical and Computers Engineering. His research interests include linear and nonlinear control theory, hybrid systems, multi-agent control systems, networked control systems, inertial navigation systems and real time architectures for complex autonomous systems with application to unmanned air, and underwater vehicles.